



Article

Performance Comparison of SOI-Based Temperature Sensors for Room-Temperature Terahertz Antenna-Coupled Bolometers: MOSFET, PN Junction Diode and Resistor

Durgadevi Elamaran ¹, Yuya Suzuki ², Hiroaki Satoh ³, Amit Banerjee ⁴ , Norihisa Hiromoto ⁵ and Hiroshi Inokawa ^{1,3,*}

¹ Graduate School of Science and Technology, Shizuoka University, Hamamatsu 432-8011, Japan; durgaelamaran@gmail.com

² Faculty of Engineering, Shizuoka University, Hamamatsu 432-8561, Japan; suzuki_yuya@fujidenki.co.jp

³ Research Institute of Electronics, Shizuoka University, Hamamatsu 432-8011, Japan; satoh.hiroaki@shizuoka.ac.jp

⁴ Physics Department, Bidhan Chandra College, Asansol 713 303, India; amitbanerjeeiacseru@gmail.com

⁵ Graduate School of Integrated Science and Technology, Shizuoka University, Hamamatsu 432-8561, Japan; hiromoto.norihisa@shizuoka.ac.jp

* Correspondence: inokawa.hiroshi@shizuoka.ac.jp

Received: 31 May 2020; Accepted: 22 July 2020; Published: 24 July 2020



Abstract: Assuming that the 0.6- μm silicon-on-insulator (SOI) complementary metal–oxide–semiconductor (CMOS) technology, different Si-based temperature sensors such as metal-oxide-semiconductor field-effect transistor (MOSFET) (n-channel and p-channel), pn-junction diode (with p-body doping and without doping), and resistors (n^+ or p^+ single crystalline Si and n^+ polycrystalline Si) were designed and characterized for its possible use in 1-THz antenna-coupled bolometers. The use of a half-wave dipole antenna connected to the heater end was assumed, which limited the integrated temperature sensor/heater area to be $15 \times 15 \mu\text{m}$. Our main focus was to evaluate the performances of the temperature sensor/heater part, and the optical coupling between the incident light and heater via an antenna was not included in the evaluation. The electrothermal feedback (ETF) effect due to the bias current was considered in the performance estimation. A comparative analysis of various SOI bolometers revealed the largest responsivity (R_v) of 5.16 kV/W for the n-channel MOSFET bolometer although the negative ETF in MOSFET reduced the R_v . The noise measurement of the n-channel MOSFET showed the NEP of 245 pW/Hz^{1/2}, which was more than one order of magnitude smaller than that of the n^+ polycrystalline Si resistive bolometer (6.59 nW/Hz^{1/2}). The present result suggests that the n-channel MOSFET can be a promising detector for THz applications.

Keywords: antenna-coupled bolometer; silicon-on-insulator (SOI); temperature sensor; responsivity (R_v); noise equivalent power (NEP); thermal response time (τ)

1. Introduction

Recently, the terahertz (THz) wave with frequencies from 0.3 to 3 THz have shown exciting possibilities in the area of non-invasive inspection and imaging for their transparency to non-polarized materials and spectral fingerprints of organic- and bio-macromolecules [1]. Compared with X-rays and millimeter waves, THz waves are non-ionizing and have a high spatial resolution. Hence, they can be effectively used for imaging concealed objects, material identification, and biomedical diagnosis [2]. Such a wide scope of the THz technology highly necessitates the development of low-cost, high sensitive,

room-temperature THz detectors. Photonic detectors operated in the THz range are inevitably affected by the small energy of the photon resulting in an additional cryogenic cooling system [3]. The recently developed semiconductor based quantum well photodetector [4], antenna-coupled silicon dot photodetector [5], and patch antenna-coupled quantum well photodetector [6] for THz detection shows a noise equivalent power (NEP) less than $1 \text{ pW/Hz}^{1/2}$ at low temperatures. Cooling requirements of photon detectors are the main obstacle for extensive usage. The possible choices of room-temperature THz detectors are microelectromechanical system (MEMS)-based resonators, electronic detectors or receivers such as the Schottky barrier diode (SBD), FET, etc., and thermal detectors such as the bolometer. Recently, GaAs based MEMS thermistors utilizing the thermo-mechanical transduction scheme were fabricated for the detection of THz radiation. The temperature change in the MEMS resonator was observed as a resonance frequency shift and realized the NEP of about $90 \text{ pW/Hz}^{1/2}$ and the operation bandwidth of several kHz simultaneously [7]. In SBD, the electric field of the incoming radiation received by an antenna is rectified by the difference between the forward and reverse flow of the current. This in turn generates a dc signal for the corresponding input power. In the case of FET, the detection of radiation results from the rectified alternating current (AC) induced by the transistor channel's nonlinear properties. The photo response that appears between the source and drain is in the form of a direct current/voltage and is proportional to the radiation power. SBD has been used for room-temperature THz detection [8], and its evolution in planar design has widened the usage [9]. Furthermore, the integration with CMOS technology realized the arrayed detectors for imaging [10]. Recently, the distributed self-mixing in the FET channel emerged as a mechanism of rectification at frequencies above its cutoff frequency [11–13], and the implementation in the CMOS platform has been studied intensively [14–18]. However, the performance of SBD and FET degrades rapidly with frequency [13], and thermal detectors, whose performance is relatively independent of frequency, become attractive at higher frequency if the temperature sensing scheme and thermal isolation structure are properly improved to attain higher performance [19]. The phenomenal thermal detector changes its material properties as a result of the temperature rise caused by the input radiation [20,21]. For a longer wavelength (λ) such as in the THz regions, due to the diffraction limits in focusing, the size of the absorber should be large in proportion to λ [20]. The realization of a large absorber and sensor with reduced thermal conductance and low heat capacity is quite difficult. To address this issue, the antenna-coupled bolometer is introduced to detect THz radiation at low frequencies. The antenna-coupled microbolometer has been extensively studied from the past three decades [22], in which the radiation signal is received by an antenna and converted to heat by the heater.

The temperature sensor is the most important element of the bolometer, and many varieties of sensors are available, such as resistor (thermistor), pn-junction diode, FET, thermocouple, etc. A wide variety of thermistor (resistor) materials such as vanadium oxide (VO_x) [23–26], metal [27–29], and semiconductors [30–33] were used in conventional absorber type bolometers. For this kind of temperature sensor, the temperature coefficient of resistance is a vital parameter. Amorphous silicon (a-Si) [33] and VO_x are the most commonly used temperature sensing materials, since they have a high temperature coefficient of resistance (TCR). However, a-Si based temperature sensor requires process optimization when integrated with a read-out circuit due to its sensitivity to the processing conditions during and after the deposition, and VO_x is not a standard material for CMOS integration, though it has a moderate TCR and resistivity. Other metals such as titanium and platinum are realized as a temperature sensor, since it has a low thermal conductivity and resistant to oxidation, respectively. On the other hand, the single crystal or polycrystalline Si has been studied extensively since it is compatible with CMOS integration. Recently, the pn-junction diode based thermal sensor has been investigated for infrared detection [34–36]. Similarly, thermocouple detectors [37] have been investigated to sense infrared radiation, the performance mainly depends on the Seebeck coefficient of the temperature sensing material. Metal-oxide-semiconductor field-effect transistor (MOSFET) bolometers, in which the threshold voltage shift by the temperature is utilized as a temperature sensing

scheme, and the amplification function of the MOSFET results in a large output, i.e., a large responsivity (R_v), have also been studied [19,38,39].

In the current work, our main focus is to compare the performance of various SOI-based temperature sensors (n/p-channel MOSFET, undoped/p⁻ body doped pn-junction diode, n⁺/p⁺ single crystalline silicon, and n⁺ polycrystalline silicon resistor) in a 1-THz antenna-coupled bolometer design [40]. Thermal detectors, including bolometers, are fundamentally limited by the temperature fluctuation noise [20,41] as will be discussed later, and NEP in the order of 100 pW/Hz^{1/2} is desirable for active imaging applications [42]. Furthermore, a high responsivity to THz radiation is beneficial since it relaxes the requirement of a low-noise amplifier in the readout circuit. In the current work, the figure of merits including R_v , NEP, and τ were evaluated and compared. To the best of our knowledge, this is the first report to make a comparison among different sensors under the common constraints of the SOI CMOS design rule.

2. Structure of Antenna-Coupled Bolometers

The main subject of this research is to evaluate and compare various temperature sensors in the 1-THz antenna-coupled bolometer design [40], where a half-wave gold dipole antenna is assumed. The common heater design is assumed with its both ends connected to the antenna rods. In such a design, the sensor/heater is placed at the center, and the length of this part should be sufficiently smaller than the total length of the antenna, i.e., 50 μm , for 1 THz. Due to the presence of the substrate with a high dielectric constant, the antenna length is shortened from the half wavelength in the free space. In the assumed design, an antenna with a width-length ratio of 0.1 is placed on a silicon substrate with the dielectric constant of 11.67, the optimum heater resistance is found to be 40 Ω [43], whereas the resistance of the gold antenna rod limited by the skin effect is 0.99 Ω at 1 THz and almost negligible. However, in the present work, the available resistance 836 Ω of the polysilicon heater is away from the optimum value, resulting in one third of the optimum absorption efficiency, and therefore only the heater/sensor component has been characterized for partial optimization.

Bolometers without an antenna of the present work were fabricated by the standard Si CMOS technology instead of the complex non-standard lift-off process used in our previously reported works [44,45]. The key advantages of the Si CMOS technology are good reproducibility and universalities of the results. For the purpose of evaluating the temperature sensor in an antenna-coupled design, the novel high performance antenna-coupled metallic microbolometer structure on a high-resistivity Si substrate for sensing at around 1 THz was adopted. This limits an integrated sensor/heater area to be 15 \times 15 μm . The minimum feature size of 0.6 μm is used in the present CMOS fabrication technology. Based on the measurement results of the fabricated device, the performance of the assumed device was estimated under the constraints of the antenna-coupled design at 1 THz and the 0.6- μm design rule. The structures of the assumed devices with its dimensions are shown in Figure 1, where a half-wave gold dipole antenna is directly coupled at both ends of the heater. The dimension of polycrystalline heater is commonly set for all the bolometers. An insulation layer stacked between an integrated sensor/heater is located at the center of an antenna, and it is suspended above the cavity in the Si substrate. The temperature sensor is electrically separated, but thermally connected with the heater. Figure 1a,b represents the assumed design of n/p-channel MOSFET and undoped/p⁻ body doped pn-junction diode bolometers, respectively. In MOSFET and diode bolometers, an additional lead with the length of 5 μm is connected on each side of its gate electrode, and it is extended towards the antenna. The gate electrode together with the lead serves as a heater. The thickness of the gate oxide, gate polysilicon, SOI, and buried oxide (BOX) are 7, 130, 100, and 200 nm, respectively. Figure 1c,d demonstrates the assumed structure of resistive bolometers with a n⁺/p⁺ single crystalline silicon thermistor and n⁺ polysilicon thermistor, respectively.

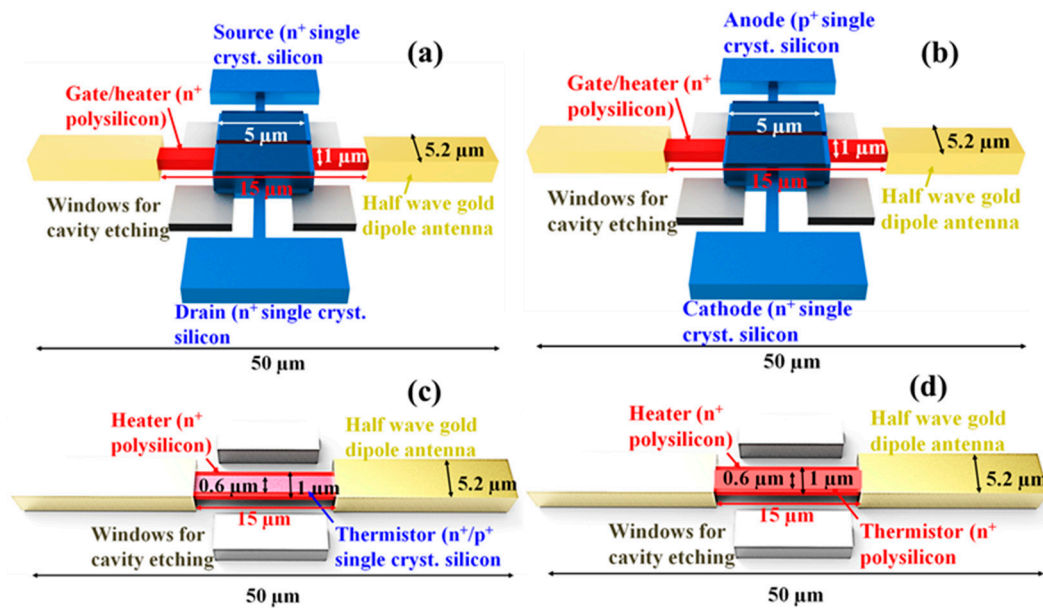


Figure 1. The structure of assumed antenna-coupled bolometers and its dimensions. (a) P or n-channel MOSFET bolometer, (b) pn-junction diode bolometer, (c) p⁺ or n⁺ single crystalline silicon resistive bolometer, and (d) n⁺ polycrystalline silicon resistive bolometer.

Table 1 represents the dimensions of the fabricated and assumed device structure. The anode/cathode width of the diode is assumed to be 5 μm. Similarly, the heater is assumed for the resistor with the width of 1 μm and length of 15 μm. Polycrystalline silicon is intended to be used as a heater material for all the bolometers. The single crystalline silicon was used to fabricate the source/drain and anode/cathode of FET and pn-junction diode, respectively. Three different kinds of Si materials such as n⁺/p⁺ single-crystal Si and n⁺ polycrystalline Si were used to fabricate the temperature sensing part of the resistive bolometer.

Table 1. Assumed device parameters and dimensions.

Parameter	Fabricated Device Dimension (μm)	Assumed Device Dimension (μm)
Heater length of metal-oxide-semiconductor field-effect transistor (MOSFET) and diode	15	15
Heater width (gate length) of MOSFET and diode	1	1
Channel width of MOSFET	5	5
Width of pn-junction diode	50	5
Thermistor length of resistive bolometer	100	15
Thermistor width of resistive bolometer	1	0.6
Heater length of resistive bolometer	100	15
Heater width of resistive bolometer	1	1
Antenna width (W_{ant})	×	5.2

× The half-wave gold dipole antenna was not fabricated.

3. Estimation Procedure of Performance Metrics

Performance metrics such as R_v , NEP, and τ of the bolometers are evaluated from the electrical response and noise measurements. The constant-current (CC) load (I_b) of 10 μA was connected to all the devices for a fair comparison among them. This section explains the procedure used to estimate various performance metrics.

3.1. Estimation Procedure of R_v

Figure 2 represents the electrical circuit for R_v estimation. R_v is the measure of output voltage at the temperature sensor for the corresponding applied sinusoidal input power (P_{in}) at the heater under constant I_b [46]. The structure and dimensions of MOSFET and diode bolometers are assumed to be the same, a similar measurement technique and modeling was used to calculate R_v . The temperature dependence of output voltage ($\Delta V_{out}/\Delta T$) was measured using a low-temperature prober Nagase Techno-Engineering Grail 21-205-6-LV-R and the Semiconductor Parameter analyzer Agilent 4156C on the fabricated devices. However, for diode bolometers the conversion has to be done on the measured results due to the variations in the device dimension. The conversion on measurement results were performed by considering the proportionality of the current to the aspect ratio (W/L). Temperature dependence of the heater input power ($\Delta T/\Delta P_{in}$) was determined by implementing analytical modeling [47]. The parameters required for analytical modeling were extracted from the measured electrical characteristics. The measured and calculated electrical and thermal parameters are shown in Table 2. Parameters used in the analytical model are electrical resistance (r_e), thermal resistance (r_t), and TCR (α) of the polysilicon heater stacked with an SiO_2 insulation layer, and thermal conductance of the source/drain or anode/cathode lead (C_c).

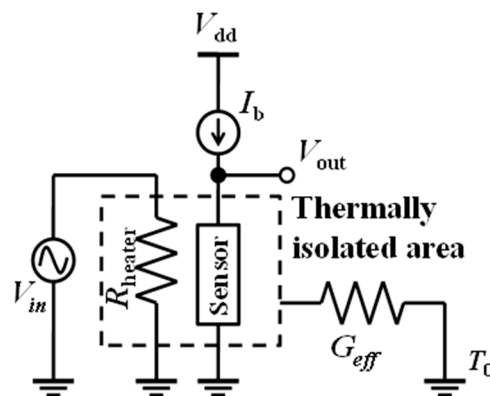


Figure 2. Equivalent circuit for responsivity (R_v) estimation.

Table 2. Measured and calculated electrical/thermal parameters. r_e and r_t are the per unit length assuming thermistor and heater dimensions shown in Table 1.

Material	Measured Electrical and Thermal Parameters			Calculated Electrical and Thermal Parameters		
	Electrical Resistance (Ω)	Thermal Conductivity k (W/mK)	Temperature Coefficient of Resistance (TCR) (K^{-1})	Electrical Resistance r_e (Ω/m)	Thermal Resistance r_t (K/Wm)	Thermal Capacitance (J/Km)
Polysilicon (Heater)// SiO_2	8.36×10^2	21.6 (poly Si) 1.38 (SiO_2)	1.11×10^{-3}	5.57×10^7	2.66×10^{11}	1.31×10^{-6}
n^+ single crystalline silicon	2.63×10^3	53.2	1.57×10^{-3}	1.75×10^8	3.13×10^{11}	9.96×10^{-5}
p^+ single crystalline silicon	1.02×10^4	53.2	9.83×10^{-4}	6.83×10^8	3.13×10^{11}	9.96×10^{-5}
Polysilicon (Thermistor)	1.44×10^3	21.6	1.15×10^{-3}	9.62×10^7	5.92×10^{11}	1.29×10^{-7}

The heater resistance was obtained from the current-voltage characteristics at room temperature. Thermal resistance can be evaluated from the slope of linear relationship between electrical resistance and square of the current. With TCR obtained from the measurement at different temperatures, thermal resistance can be extracted explicitly [48]. If there is a branch of thermal conduction [47], such as source/drain leads, the thermal conductance C_c can be obtained as a fitting parameter to reproduce the results from the samples with different dimensions. Reported values of specific heat,

$1.6 \times 10^6 \text{ J/Km}^3$ [49] for SiO_2 and $1.66 \times 10^6 \text{ J/Km}^3$ [50] for Si, were used to estimate the thermal capacitance and the response time (τ) of the bolometers.

Finally, R_v is evaluated from the temperature dependence of output voltage and input power as $R_v = (\Delta V_{out}/\Delta T) \times (\Delta T/\Delta P_{in})$. The temperature rise of FET bolometer is observed as a change in the gate threshold voltage ($\Delta V_{gth}/\Delta T$). The amplification factors ($g_m R_o$) are then multiplied with ($\Delta V_{gth}/\Delta T$) to get the final output response, where g_m is the transconductance calculated from the drain current-gate voltage characteristics at $10 \mu\text{A}$, and R_o is the output resistance obtained from the drain current-drain voltage characteristics at the drain voltage of 1 V. Similarly, in the diode bolometers, the change in the forward bias voltage ($\Delta V_f/\Delta T$) was measured as a function of temperature.

Electrothermal simulation was carried out using the SPICE circuit simulator to evaluate the R_v of resistive bolometers [51] due to the lack of the fabricated device. Figure 3a represents a unit circuit of heater/thermistor with length ΔL , TCR (α), r_e , r_t , and c_t . The entire circuit is depicted in Figure 3b in which the heater/sensor is stacked parallel. A bias current of $10 \mu\text{A}$ is applied to the temperature sensor. Temperature sensor parameters were extracted from the electrical measurements performed on the fabricated structure. Conversion from the fabricated device to the assumed device (length = $15 \mu\text{m}$ and width = $0.6 \mu\text{m}$) was done by assuming the identical resistivity between them. The transient analysis was performed with a sinusoidal input under the CC bias of $10 \mu\text{A}$ in the SPICE circuit simulator for converting the temperature amplitude to the temperature sensor output voltage.

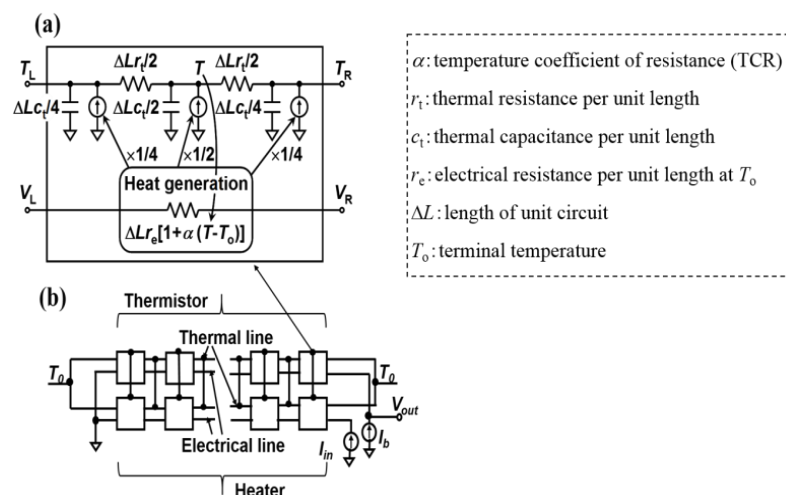


Figure 3. (a) Unit and (b) entire circuits of resistive bolometers for electrothermal simulation [51].

3.2. Estimation Procedure of Noise Equivalent Power (NEP) and Thermal Response Time (τ)

An important performance metric of thermal detectors is its NEP, which is defined as the input power that gives a signal-to-noise ratio of one for the output noise per unit bandwidth. Figure 4 represents the measurement setup for estimating voltage noise. The device being tested is mounted in the Nagase Techno-Engineering Grail 21-205-6-LV-R room temperature prober. The Agilent 35670A FFT dynamic signal analyzer has been used to measure the power spectral density of output voltage noise over a frequency range of 1 to 100 kHz together with the DL Instruments model 1201 low-noise voltage preamplifier with a gain of 100 and input-referred noise of less than $15 \text{ nV/Hz}^{1/2}$ at 10 Hz. The input from the bolometer and the output of the amplifier were AC coupled to prevent overdriving the input of the spectrum analyzer due to the DC offset induced by I_b .

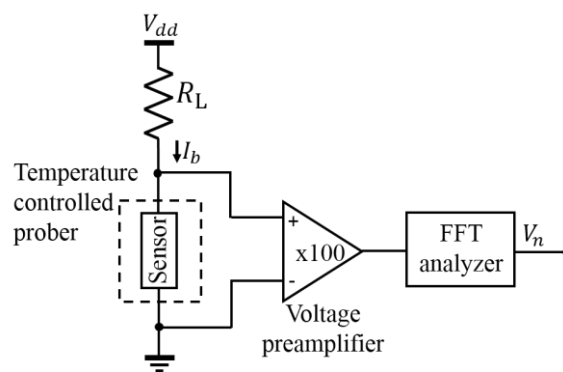


Figure 4. Circuit for noise measurement.

For the estimation of R_v we considered the CC load instead of the resistor load. However, for the noise measurement, the metal-film resistor R_L is connected as the load because the available CC load is noisy. The constant bias current of $10 \mu\text{A}$ was maintained by assuming the same current density for both fabricated and assumed bolometers. Since the dimensions of the measured and assumed bolometers are different and the loads are different, the output noise voltages of the measured bolometers are converted by the procedures explained in Appendix A. NEP is calculated from the estimated voltage noise (V_n) at 10 Hz divided by R_v . NEP in terms of $\text{W}/\text{Hz}^{1/2}$ is expressed as:

$$NEP = \frac{V_n}{R_v} \quad (1)$$

The bolometer response time or thermal time constant (τ) is generally expressed as the heat capacity (C) divided by thermal conductance (G). The measured cutoff frequency (f_c) can be directly related to the τ . The R_v of n-channel MOSFET was measured from the identical test structures by applying an amplitude-modulated input signal with the carrier frequency of 5 MHz and various modulation frequency (f_m) to the heater to realize the flat response of the measurement system with respect to f_m up to 100 kHz. The fundamental or second-harmonic output voltage (f_m or $2f_m$) was recorded using a lock-in amplifier because the temperature rise is proportional to the square of the temporal amplitude of the modulated signal. The τ of the p-channel MOSFET and diode bolometers was obtained only by the compensation of the electrothermal feedback effect, which will be discussed later, since MOSFET and diode bolometers have the same structure except for the doping conditions. An electro thermal simulation based on the extracted parameters was carried out to evaluate the f_c of resistive bolometers.

4. Results and Discussion

As explained in Section 3, all the characterization was performed under the CC bias of $10 \mu\text{A}$. The temperature rise in the bolometer due to the bias current crucially affects the performance metrics such as R_v and τ due to the Joule self-heating through the positive TCR. According to [20], the effective thermal conductance G_e modified by this electrothermal feedback (ETF) effect can be expressed for resistive bolometers with a constant-current load as:

$$G_e = G_0\{1 - (T_1 - T_0)\alpha\}, \quad (2)$$

where T_1 and T_0 are the bolometer and ambient temperatures, respectively. For a positive TCR (α), as in the case of metallic resistors, the positive feedback results in the smaller G_e and enhanced responsivity R_v . The second term $(T_1 - T_0)\alpha$ shows the extent of the effect.

As for the diode and MOSFET bolometers, effective TCR (α) can be defined respectively as:

$$\alpha = (\Delta V_f / \Delta T) / V_f \quad (3)$$

And

$$\alpha = (\Delta V_{gth}/\Delta T) \times (g_m R_o)/V_d, \quad (4)$$

where V_f and V_d are the forward bias (anode) and drain voltages during operation, respectively.

Table 3 summarizes the extent of the ETF effect. Since the threshold voltage V_{gth} of MOSFET and V_f of diode has negative temperature coefficients, the negative feedback, i.e., reduction of the R_v and increase in the τ , arises. It can be seen that the n- and p-channel MOSFET bolometers are affected appreciably, and others are not. Note that this effect is automatically included in the electrothermal simulation for resistive bolometers, but the effect on MOSFET and diode bolometers is compensated after the estimation of the R_v .

Table 3. Extent of the electrothermal feedback (ETF) effect. The temperature coefficient of resistances (TCRs) for MOSFETs and diodes are effective values.

Bolometers	$T_1 - T_0$ (K)	TCR (K ⁻¹)	$(T_1 - T_0)\alpha$ (%)
N-channel MOSFET	2.86	-6.18×10^{-2}	-17.6
P-channel MOSFET	2.86	-1.71×10^{-2}	-4.9
Diode (without body doping)	2.53	-1.22×10^{-3}	-0.31
Diode (with p-body doping)	2.53	-1.19×10^{-3}	-0.30
Resistive (n ⁺ single crystalline Si)	4.74×10^{-2}	1.57×10^{-3}	~0
Resistive (p ⁺ single crystalline Si)	1.85×10^{-1}	9.83×10^{-4}	~0
Resistive (polycrystalline Si)	3.32×10^{-2}	1.15×10^{-3}	~0

The R_v of MOSFET and diode bolometers before compensation of the ETF effect is estimated from the electrical measurement and analytical modeling. The gate threshold voltage shift and forward bias voltage shift take place as a result of the applied heater input power to MOSFET and diode bolometers, respectively. In the present MOSFET and diode bolometers, the input signal is applied to the heater (gate) and the resultant output signal is measured at the drain/anode under a constant bias current of 10 μ A. Temperature dependence of the heater input power ($\Delta T/\Delta P_{in} = 1.43 \times 10^5$ K/W) was evaluated by implementing analytical modeling. Since the common heater is assumed, the same value is used for the diode bolometer. Figure 5a,b represents the $I_d - V_g$ and $I_d - V_d$ characteristics of the MOSFET bolometer, respectively. Transconductance (g_m) and output conductance (g_o) required to calculate the amplification factor of MOSFET bolometers are extracted at 10 μ A of the drain current (or bias current) and at 1 V of the drain voltage, respectively. The resultant amplification factors are 122 and 20.8 for the n and p-channel MOSFET, respectively. Temperature dependence of the gate threshold voltage ($\Delta V_{gth}/\Delta T$) and forward bias voltage ($\Delta V_f/\Delta T$) of MOSFET and diode bolometers are shown in Figure 6a,b, respectively. The $\Delta T/\Delta P_{in}$ and $\Delta V_{gth}/\Delta T$ together with the amplification factor gives the R_v of MOSFET bolometer. Similarly, the $\Delta T/\Delta P_{in}$ and $\Delta V_f/\Delta T$ was used to compute the R_v of diode bolometer. The R_v of resistive bolometers were simulated based on the electrothermal circuit. Figure 7 presents the comparison of R_v for the studied bolometers. The highest R_v was attained by the n-channel MOSFET bolometer, which is three orders of magnitude higher than those of the resistive bolometers.

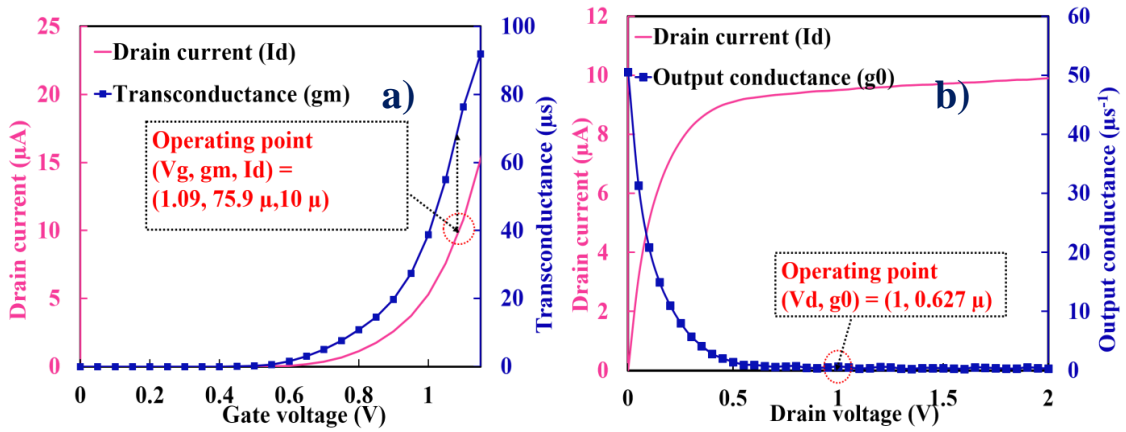


Figure 5. (a) Extraction of the transconductance (g_m) from drain current vs. gate voltage characteristics; (b) extraction of the output conductance (g_0) from drain current vs. drain voltage characteristics. As an example, characteristics of the n-channel MOSFET with $L = 1 \mu\text{m}$ and $W = 5 \mu\text{m}$ are shown. $V_d = 1.00 \text{ V}$ for (a), and $V_g = 1.09 \text{ V}$ for (b).

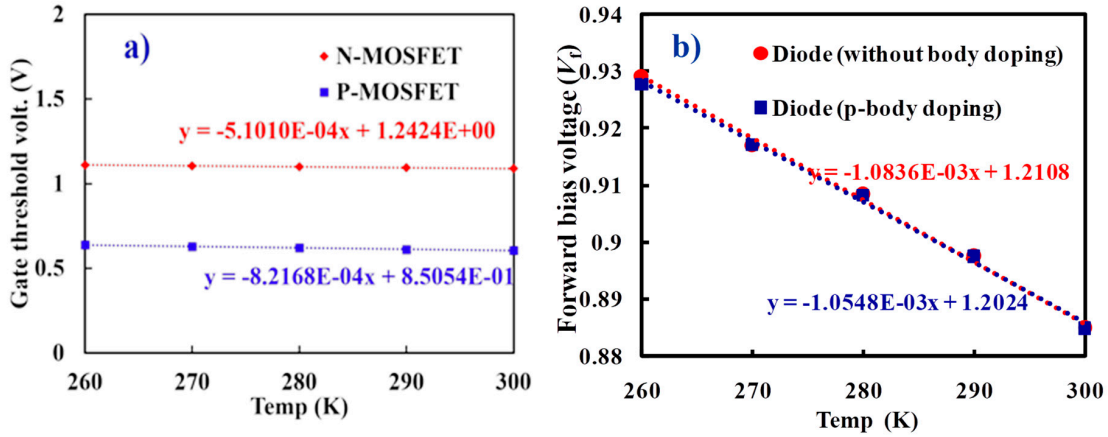


Figure 6. (a) Temperature dependence of the gate threshold voltage (MOSFET bolometer), and (b) temperature dependence of the forward bias voltage (diode bolometer).

The NEPs limited by the temperature fluctuation noise (thermal Johnson-Nyquist noise), and background fluctuation noise (photon noise) can be estimated as follows [20]:

$$NEP_{TF} = (4k_B T^2 G)^{1/2}, \tag{5}$$

And

$$NEP_{BF} = (16A_e \sigma k_B T^5)^{1/2}, \tag{6}$$

where k_B , T , G , A_e , and σ are the Boltzman constant, temperature, thermal conductance, effective area of detector, and Stefan-Boltzman constant, respectively. Since the Gs for the present MOSFET/diode bolometer, the n^+/p^+ single crystalline, and n^+ poly crystalline resistive bolometers are 3.5, 5.5, and $4.3 \mu\text{W/K}$, the NEP_{TF} s at 300 K are 4.2, 5.2, and $4.6 \text{ pW/Hz}^{1/2}$, respectively. If we assume the bolometers coupled with a half-wave dipole antenna [52] $A_e \sim 0.13\lambda^2$, then NEP_{BF} is calculated to be $0.6 \text{ pW/Hz}^{1/2}$ at 300 K for the 1-THz operation. Since these NEPs are not dominant in the present bolometers, we will focus on the noises of the temperature sensors.

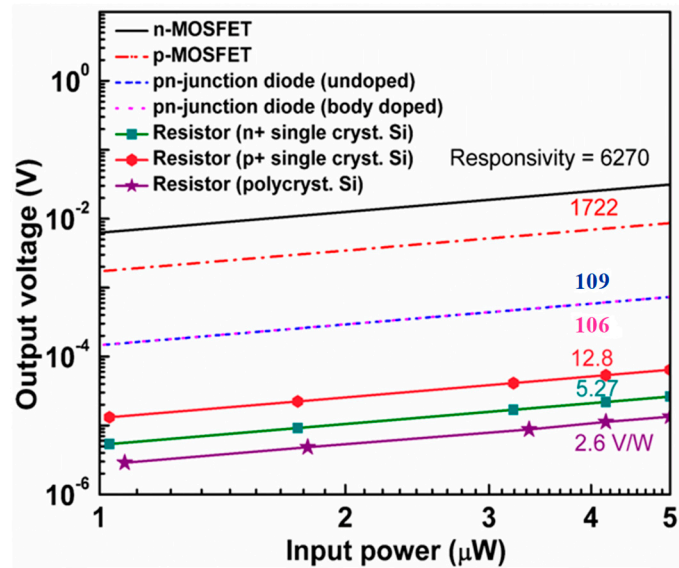


Figure 7. Estimated output voltage response of various bolometers for the heater input power. The ETF effect is not included in the lines for MOSFET and diode bolometers.

The voltage noise power spectral density (PSDs) of various bolometers are shown in Figure 8. Since the noise of MOSFETs shows a flicker or Lorentzian noise-like $1/f^n$ increase at low frequencies, noise levels at 10 Hz (near the corner frequency) are chosen to evaluate the NEP. This frequency is covered by the measurements with stop frequencies of 12.5 and 200 Hz, and the number of data points of 400. Although the equivalent noise band widths [53] are 47 and 750 mHz, respectively, the same PSDs are obtained at 10 Hz, indicating that the NEPs are not affected by the $1/f^n$ behavior as long as the band width for the noise measurement is narrow. Spikes in the noise spectrum are due to the environmental noise. The baseline white noise is the thermal noise for MOSFETs and resistive thermistors, and shot noise for diodes. In the low-frequency region, the excess $1/f^n$ noise is superimposed. The roll-off at a high frequency is caused by the limited band width of the measurement system.

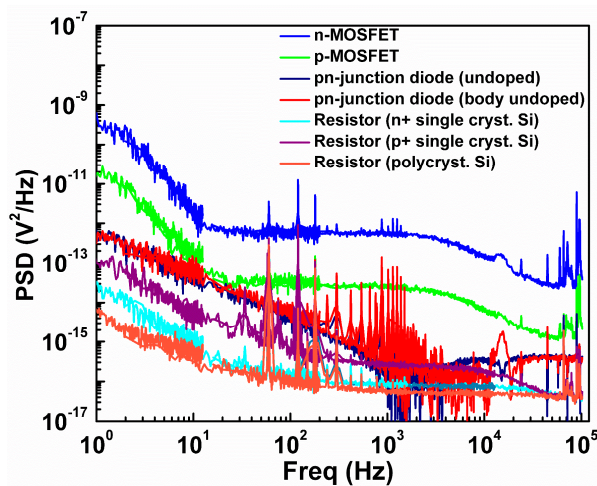


Figure 8. Voltage noise power spectral density (PSD) of investigated bolometers.

Table 4 summarizes R_v , NEP, and τ , in which the ETF effect is included. The noise equivalent temperature difference (NETD) is also calculated for the ease of comparison with other temperature sensors. Compared to the values in Figure 7, the R_v of MOSFET bolometers, especially the n-channel MOSFET, gets degraded due to the ETF effect. Nevertheless, the n-channel MOSFET bolometer, which exhibits six times higher voltage gain compared to the p-channel one, shows the largest R_v

of 5.16 kV/W due to the large amplifying function. The p-channel MOSFET bolometer attains the smallest NEP as the result of the superior trade-off between R_v and noise. This can be explained by its low input-referred noise related to the buried-channel operation as a result of n-type channel doping with the n^+ polysilicon gate. The resistive bolometers show that the noise voltage is smaller than those of other bolometers, but the NEP is worse due to the poor R_v . Resistive bolometers with the n^+/p^+ single crystalline silicon thermistor have the smallest τ of 2.34 μ s. Generally, the τ s obtained in this study are short, promising the operation band width of more than several kHz. For imaging applications, in which the ordinary frame rate is \sim 60 fps, there is a room for the improvement of R_v by mitigating the response speed. The NETD as small as 23.1 μ K/Hz^{1/2} is attained by the p-channel MOSFET, which results in the resolution figure-of-merit of 5.3 fJ·K² comparable to 2.3 fJ·K² by the state-of-the-art temperature sensor [54].

Table 4. Performance comparison among the studied bolometers. The ETF effect is considered in R_v , noise equivalent power (NEP), and τ , but is not in the noise equivalent temperature difference (NETD) based on the assumption of isothermal measurement.

Bolometers	Voltage Noise at 10 Hz (V/Hz ^{1/2})	Responsivity R_v (V/W)	NEP (W/Hz ^{1/2})	Response Time τ (μ s)	NETD (K/Hz ^{1/2})
N-channel MOSFET	1.27×10^{-6}	5.16 k	2.45×10^{-10}	13.8	2.88×10^{-5}
P-channel MOSFET	2.79×10^{-7}	1.64 k	1.70×10^{-10}	15.9	2.31×10^{-5}
Diode (without body doping)	2.08×10^{-7}	109	1.99×10^{-9}	16.7	2.83×10^{-4}
Diode (with p- doping)	2.27×10^{-7}	106	2.15×10^{-9}	16.7	3.05×10^{-4}
Resistive (n^+ single-Si)	2.70×10^{-8}	5.27	5.12×10^{-9}	2.34	9.23×10^{-4}
Resistive (p^+ single-Si)	7.72×10^{-8}	12.8	6.01×10^{-9}	2.34	1.07×10^{-3}
Resistive (n^+ poly-Si)	1.78×10^{-8}	2.69	6.59×10^{-9}	3.07	1.52×10^{-3}

5. Conclusions

In this work, the main intension is to evaluate the performance of different Si-based temperature sensors integrated in antenna-coupled bolometers. To the best of our knowledge, this is the first report to make a fair comparison among different sensors under the common constraints of the silicon-on-insulator (SOI) CMOS design rule. The performances in terms of R_v , NEP, and τ were evaluated for various temperature sensors such as MOSFETs (n- and p-channel), pn-junction diodes (with and without body doping), and resistors with different materials (n^+ and p^+ single-crystal Si, and n^+ polycrystalline Si) for a 1-THz antenna-coupled bolometer. The ETF effect due to the bias current affected the performance of MOSFET bolometers appreciably. Even though, the n-channel MOSFET showed the largest R_v of 5.16 kV/W. The high R_v was mainly due to the signal amplifying function of the MOSFET. In addition, as the general characteristics of thin (\sim 100 nm) SOI material, the reduced thermal conductance due to the enhanced phonon scattering could also contribute to the larger temperature rise, higher R_v , and smaller NEP [48,55]. As the result of better compatibility between low noise and high R_v , the p-channel MOSFET bolometer showed the smallest NEP of 170 pW/Hz^{1/2} at 10 Hz. Currently, the contribution of the thermal Johnson-Nyquist noise and the photon noise is not dominant, but would become an issue if we consider the passive imaging, in which NEP less than a few pW/Hz^{1/2} is required. The smallest thermal response time τ of 2.34 μ s was attained by the n^+/p^+ resistive bolometers, whereas the n-channel MOSFET has the τ of 13.8 μ s. For imaging applications, still there is a room for improvement in R_v by sacrificing the τ to the level of ordinary video frame rate. Considering the overall performance, i.e., high R_v (high output voltage), moderate

NEP, and τ , it can be concluded that the n-channel MOSFET at the center of an antenna can be a promising detector for the electromagnetic waves around 1 THz, which is useful for transparent imaging and material identification.

Author Contributions: Conceptualization, device design, and arrangement of the device fabrication, H.I.; device measurement, analysis and interpretation of the data, and drafting the manuscript, D.E.; preliminary measurement and the thermal conductance analysis of the FET bolometers, Y.S.; verification of the analysis and the manuscript, H.I., H.S., A.B., and N.H. All authors have read and agreed to the published version of the manuscript.

Funding: This research was funded by the Cooperative Research Project of the Research Center for Biomedical Engineering with the Research Institute of Electronics, Shizuoka University, and the Cooperative Research Project Program of RIEC, Tohoku University.

Acknowledgments: The authors are indebted to the Solid State Division of Hamamatsu Photonics K.K. for providing the SOI CMOS devices before fabrication of the cavity.

Conflicts of Interest: The authors declare no conflict of interest.

Appendix A Conversion Procedure of the Output Noise Voltages

MOSFET Bolometer

For the FET bolometer, an input referred noise is estimated from the measured noise ($\overline{V_{n,meas}^2}$) divided by the voltage gain ($A_{v,meas}$) with load resistance R_L and can be expressed as:

$$\overline{V_{in,meas}^2} = \frac{\overline{V_{n,meas}^2}}{(A_{v,meas})^2} \quad (A1)$$

The voltage gain of the FET including the load resistor R_L is expressed as:

$$A_{v,meas} = g_m \cdot (R_{meas} \parallel R_L) \quad (A2)$$

The CC load voltage noise ($\overline{V_{n,est}^2}$) is then calculated by multiplying the input referred noise ($\overline{V_{in,meas}^2}$) with the voltage gain ($A_{v,est}$) without R_L which can be written as:

$$\overline{V_{n,est}^2} = \overline{V_{in,meas}^2} \cdot (A_{v,est})^2 \quad (A3)$$

$$A_{v,est} = g_m \cdot R_{meas} \quad (A4)$$

Diode and Resistive Bolometer

The noise voltage of the assumed diode and resistive bolometer at the CC load was estimated based on the circuit diagram shown in Figure A1.

For the pn-junction diode bolometer, noise has been estimated by considering both shot noise and thermal noise. The effect of R_L was eliminated by subtracting the theoretical thermal noise from the measured noise, which can be expressed as:

$$\overline{V_{n,meas}^2(\text{without } RL)} = \overline{V_{n,meas}^2(\text{with } RL)} - \overline{V_{n,RL}^2} \quad (A5)$$

Since the shot noise originates from the electric charge, the measured voltage noise was converted to the current noise for further conversion. The assumed diode bolometer current noise ($\overline{I_{n,est}^2}$) can be expressed as:

$$\overline{I_{n,est}^2} = \left\{ \frac{\frac{4kT}{R_{meas}} + 2qI_{b,meas}}{\frac{4kT}{R_{est}} + 2qI_{b,est}} \right\} \cdot \overline{V_{n,meas}^2} \quad (A6)$$

The current noise of the diode bolometer is converted to voltage noise by:

$$\overline{V_{n,est}^2} = \overline{I_{n,est}^2} \cdot (R_{est})^2 \quad (\text{A7})$$

$I_{b,meas}$ and $I_{b,est}$ are the bias currents of fabricated and assumed devices, respectively. Similarly, R_{meas} and R_{est} are resistances of fabricated and assumed diode bolometers.

For the resistive bolometer in which the thermal noise is of major concern the conversion equation can be written as:

$$\overline{V_{n,est}^2} = \overline{V_{n,meas}^2} \cdot \left\{ \frac{R_{est}}{R_{meas} || R_L} \right\} \quad (\text{A8})$$

where R_{meas} and R_{est} are the resistances of fabricated and assumed devices, respectively.

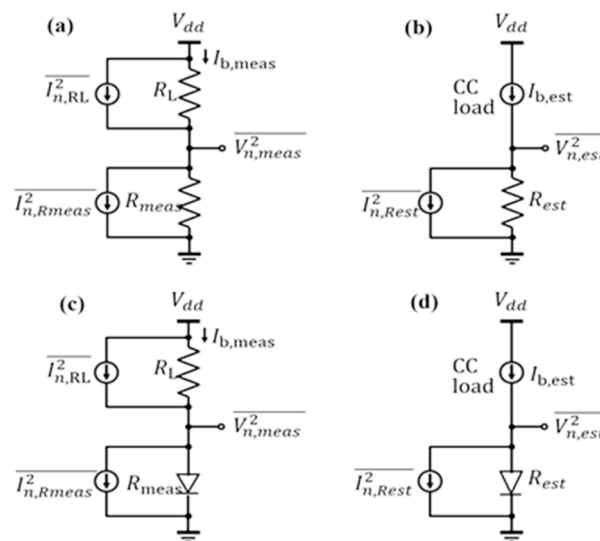


Figure A1. Noise modeling for the measured (fabricated) and estimated (assumed) bolometers. (a) Measured noise for the available resistive bolometer with a resistive load, (b) estimated noise for the designed resistive bolometer with a CC load, (c) measured noise for the available diode bolometer with a resistive load, (d) estimated noise for the designed diode bolometer with a CC load.

References

1. Kukutsu, N.; Kado, Y. Overview of millimeter and terahertz wave application research. *NTT Tech. Rev.* **2009**, *7*, 1–6.
2. Zhu, B.; Chen, Y.; Deng, K.; Hu, W.; Yao, Z.S. Terahertz Science and Technology and Applications. *PIERS Proc.* **2009**, *2*, 1166–1170.
3. Rogalski, A. Infrared thermal detectors versus photon detectors: I. Pixel performance. *Mater. Sci. Mater. Prop. Infrared Optoelectron.* **1997**, *3182*, 14–25. [[CrossRef](#)]
4. Li, H.; Wan, W.J.; Tan, Z.Y.; Fu, Z.L.; Wang, H.X.; Zhou, T.; Li, Z.P.; Wang, C.; Guo, X.G.; Cao, J.C. 6.2-GHz modulated terahertz light detection using fast terahertz quantum well photodetectors. *Sci. Rep.* **2017**, *7*, 3452. [[CrossRef](#)] [[PubMed](#)]
5. Okamoto, T.; Fujimura, N.; Crespi, L.; Kodera, T.; Kawano, Y. Terahertz detection with an antenna-coupled highly-doped silicon quantum dot. *Sci. Rep.* **2019**, *9*, 18574. [[CrossRef](#)]
6. Palaferri, D.; Todorov, Y.; Chen, Y.N.; Madeo, J.; Vasanelli, A.; Li, L.H.; Davies, A.G.; Linfield, E.H.; Sirtori, C. Patch antenna terahertz photodetectors. *Appl. Phys. Lett.* **2015**, *106*, 161102. [[CrossRef](#)]
7. Zhang, Y.; Hosono, S.; Nagai, N.; Song, S.-H.; Hirakawa, K. Fast and sensitive bolometric terahertz detection at room temperature through thermomechanical transduction. *J. Appl. Phys.* **2019**, *125*, 151602. [[CrossRef](#)]
8. Kreisler, A.J.M. Submillimeter Wave Applications of Submicron Schottky Diodes. *Far-Infrared Sci. Technol.* **1986**, *666*, 51–63. [[CrossRef](#)]

9. Crowe, T.W.; Mattauch, R.J.; Weikle, R.M.; Bhapkar, U.V. Terahertz Gaas Devices and Circuits for Heterodyne Receiver Applications. *Int. J. High. Speed Electron. Syst.* **1995**, *6*, 125–161. [[CrossRef](#)]
10. Han, R.; Zhang, Y.; Kim, Y.; Kim, D.Y.; Shichijo, H.; Afshari, E.; Kenneth, K.O. Active Terahertz Imaging Using Schottky Diodes in CMOS: Array and 860-GHz Pixel. *IEEE J. Solid-State Circuits* **2013**, *48*, 2296–2308. [[CrossRef](#)]
11. Knap, W.; Teppe, F.; Meziani, Y.; Dyakonova, N.; Lusakowski, J.; Boeuf, F.; Skotnicki, T.; Maude, D.; Rumyantsev, S.; Shur, M.S. Plasma wave detection of sub-terahertz and terahertz radiation by silicon field-effect transistors. *Appl. Phys. Lett.* **2004**, *85*, 675–677. [[CrossRef](#)]
12. Tauk, R.; Teppe, F.; Boubanga, S.; Coquillat, D.; Knap, W.; Meziani, Y.M.; Gallon, C.; Boeuf, F.; Skotnicki, T.; Fenouillet-Beranger, C.; et al. Plasma wave detection of terahertz radiation by silicon field effects transistors: Responsivity and noise equivalent power. *Appl. Phys. Lett.* **2006**, *89*, 253511. [[CrossRef](#)]
13. Golenkov, A.G.; Sizov, F.F. Performance limits of terahertz zero biased rectifying detectors for direct detection. *Semicond. Phys. Quantum Electron. Optoelectron.* **2016**, *19*, 129–138. [[CrossRef](#)]
14. Földesy, P.; Gergelyi, D.; Füzy, C.; Károlyi, G. Test and configuration architecture of a sub-THz CMOS detector array. In Proceedings of the 15th International Symposium on Design and Diagnostics of Electronic Circuits & Systems (DDECS), Tallinn, Estonia, 15–20 April 2012; pp. 101–104. [[CrossRef](#)]
15. Bauer, M.; Boppel, S.; Lisauskas, A.; Krozer, V.; Roskos, H.G. Real-time CMOS terahertz camera employing plane-to-plane imaging with a focal-plane array of field-effect transistors. In Proceedings of the 38th International Conference on Infrared, Millimeter, and Terahertz Waves (IRMMW-THz), Mainz, Germany, 1–6 September 2013; pp. 2–3. [[CrossRef](#)]
16. Perenzoni, D.; Perenzoni, M.; Gonzo, L.; Capobianco, A.D.; Sacchetto, F. Analysis and design of a CMOS-based terahertz sensor and readout. *Opt. Sens. Detect.* **2010**, 7726, 772618. [[CrossRef](#)]
17. Schuster, F.; Coquillat, D.; Videlier, H.; Sakowicz, M.; Teppe, F.; Dussopt, L.; Giffard, B.; Skotnicki, T.; Knap, W. Broadband terahertz imaging with highly sensitive silicon CMOS detectors. *Opt. Express* **2011**, *19*, 7827–7832. [[CrossRef](#)] [[PubMed](#)]
18. Lisauskas, A.; Boppel, S.; Roskos, H.G.; Matukas, J.; Palenskis, V.; Minkevičius, L.; Valušis, G.; Haring Bolivar, P. Terahertz responsivity enhancement and low-frequency noise study in silicon CMOS detectors using a drain current bias. In Proceedings of the 21st International Conference on Noise and Fluctuations, Toronto, ON, Canada, 12–16 June 2011; pp. 297–300. [[CrossRef](#)]
19. Nemirovsky, Y.; Svetlitz, A.; Brouk, I.; Stolyarova, S. Nanometric CMOS-SOI-NEMS transistor for uncooled THz sensing. *IEEE Trans. Electron. Devices* **2013**, *60*, 1575–1583. [[CrossRef](#)]
20. Kruse, P.W. *Uncooled Thermal Imaging. Arrays, Systems, and Applications*; SPIE: Bellingham, WA, USA, 2001.
21. Garn, L.E. Fundamental noise limits of thermal detectors. *J. Appl. Phys.* **1984**, *55*, 1243–1253. [[CrossRef](#)]
22. Neikirk, D.P.; Lam, W.W.; Rutledge, D.B. Far-infrared microbolometer detectors. *Int. J. Infrared Millim. Waves* **1984**, *5*, 245–278. [[CrossRef](#)]
23. Chen, S.; Ma, H.; Xiang, S.; Yi, X. Fabrication and performance of microbolometer arrays based on nanostructured vanadium oxide thin films. *Smart Mater. Struct.* **2007**, *16*, 696–700. [[CrossRef](#)]
24. Chen, C.; Yi, X.; Zhao, X.; Xiong, B. Characterizations of VO₂-based uncooled microbolometer linear array. *Sensors Actuators A Phys.* **2001**, *90*, 212–214. [[CrossRef](#)]
25. Chen, C.; Yi, X.; Zhang, J.; Zhao, X. Linear uncooled microbolometer array based on VO_x thin films. *Infrared Phys. Technol.* **2001**, *42*, 87–90. [[CrossRef](#)]
26. Wang, H.; Yi, X.; Huang, G.; Xiao, J.; Li, X.; Chen, S. IR microbolometer with self-supporting structure operating at room temperature. *Infrared Phys. Technol.* **2004**, *45*, 53–57. [[CrossRef](#)]
27. Bhan, R.K.; Saxena, R.S.; Jalwania, C.R.; Lomash, S.K. Uncooled infrared microbolometer arrays and their characterisation techniques. *Def. Sci. J.* **2009**, *59*, 580–589. [[CrossRef](#)]
28. Lee, H.K.; Yoon, J.B.; Yoon, E.; Ju, S.B.; Yong, Y.J.; Lee, W.; Kim, S.G. A high fill-factor infrared bolometer using micromachined multilevel electrothermal structures. *IEEE Trans. Electron. Devices* **1999**, *46*, 1489–1491. [[CrossRef](#)]
29. Banerjee, A.; Satoh, H.; Sharma, Y.; Hiromoto, N.; Inokawa, H. Characterization of platinum and titanium thermistors for terahertz antenna-coupled bolometer applications. *Sens. Actuators A Phys.* **2018**, *273*, 49–57. [[CrossRef](#)]
30. Tezcan, D.S.; Eminoglu, S.; Akin, T. A low-cost uncooled infrared microbolometer detector in standard CMOS technology. *IEEE Trans. Electron. Devices* **2003**, *50*, 494–502. [[CrossRef](#)]

31. Niklaus, F.; Kälvesten, E.; Stemme, G. Wafer-level membrane transfer bonding of polycrystalline silicon bolometers for use in infrared focal plane arrays. *J. Micromech. Microeng.* **2001**, *11*, 509–513. [[CrossRef](#)]
32. Niklaus, F.; Pejnefors, J.; Dainese, M.; Haggblad, M.; Hellstrom, P.E.; Wallgren, U.J.; Stemme, G. Characterization of transfer-bonded silicon bolometer arrays. *Proc. SPIE* **2004**, *5406*, 521–530. [[CrossRef](#)]
33. Simoens, F.; Meilhan, J. Terahertz real-time imaging uncooled array based on antenna- and cavity-coupled bolometers. *Philos. Trans. R. Soc. A Math. Phys. Eng. Sci.* **2014**, *372*, 20130111. [[CrossRef](#)]
34. Ueno, M.; Kosasayama, Y.; Sugino, T.; Nakaki, Y.; Fujii, Y.; Inoue, H.; Kama, K.; Seto, T.; Takeda, M.; Kimata, M. 640 × 480 pixel uncooled infrared FPA with SOI diode detectors. *Proc. SPIE* **2005**, *5783*, 566–577. [[CrossRef](#)]
35. Ishikawa, T.; Ueno, M.; Nakaki, Y.; Endo, K.; Ohta, Y.; Nakanishi, J.; Kosasayama, Y.; Yagi, H.; Sone, T.; Kimata, M. Performance of 320 × 240 uncooled IRFPA with SOI diode detectors. *Proc. SPIE* **2000**, *4130*, 152–159. [[CrossRef](#)]
36. Kimata, M.; Ueno, M.; Takeda, M.; Seto, T. SOI diode uncooled infrared focal plane arrays. *Proc. SPIE* **2006**, *6127*, 61270X. [[CrossRef](#)]
37. Olgun, Z.; Akar, O.; Kulah, H.; Akin, T. An integrated thermopile structure with high responsivity using any standard CMOS process. In Proceedings of the International Solid State Sensors and Actuators Conference (Transducers'97), Chicago, IL, USA, 19 June 1997; pp. 1263–1266. [[CrossRef](#)]
38. Gitelman, L.; Stolyarova, S.; Bar-Lev, S.; Gutman, Z.; Ochana, Y.; Nemirovsky, Y. CMOS-SOI-MEMS transistor for uncooled IR imaging. *IEEE Trans. Electron. Devices* **2009**, *56*, 1935–1942. [[CrossRef](#)]
39. Morf, T.; Klein, B.; Despont, M.; Drechsler, U.; Kull, L.; Corcos, D.; Elad, D.; Kaminski, N.; Pfeiffer, U.R.; Al Hadi, R.; et al. Wide bandwidth room-temperature THz imaging array based on antenna-coupled MOSFET bolometer. *Sensors Actuators A Phys.* **2014**, *215*, 96–104. [[CrossRef](#)]
40. Hiromoto, N.; Tiwari, A.; Aoki, M.; Satoh, H.; Takeda, M.; Inokawa, H. Room-temperature THz antenna-coupled microbolometer with a Joule-heating resistor at the center of a half-wave antenna. In Proceedings of the 38th International Conference on Infrared, Millimeter, and Terahertz Waves (IRMMW-THz), Tucson, AZ, USA, 14–19 September 2014; pp. 1–2. [[CrossRef](#)]
41. Kruse, P.W. A comparison of the limits to the performance of thermal and photon detector imaging arrays. *Infrared Phys. Technol.* **1995**, *36*, 869–882. [[CrossRef](#)]
42. Rogalski, A. New trends in infrared and terahertz detectors. In Proceedings of the Conference on Optoelectronic and Microelectronic Materials & Devices, Perth, Australia, 14–17 December 2014; pp. 218–220. [[CrossRef](#)]
43. Kominami, M.; Pozar, D.M.; Schaubert, D.H. Dipole and slot elements and arrays on semi-infinite substrate. *IEEE Trans. Antennas Propag.* **1985**, *33*, 600–607. [[CrossRef](#)]
44. Banerjee, A.; Satoh, H.; Tiwari, A.; Apriono, C.; Rahardjo, E.T.; Hiromoto, N.; Inokawa, H. Width dependence of platinum and titanium thermistor characteristics for application in room-temperature antenna-coupled terahertz microbolometer. *Jpn. J. Appl. Phys.* **2017**, *56*, 04CC07. [[CrossRef](#)]
45. Tiwari, A.; Satoh, H.; Aoki, M.; Takeda, M.; Hiromoto, N.; Inokawa, H. THz Antenna-Coupled Microbolometer with 0.1- μm -wide Titanium Thermistor. *Intern. J. ChemTech Res.* **2015**, *7*, 1019–1026.
46. Datskos, P.G.; Lavrik, N.V. Detector—figure of merits. In *Encyclopedia of Optical Engineering*; Driggers, R.G., Ed.; Marcel Dekker Inc.: New York, NY, USA, 2003; p. 349.
47. Tiwari, A.; Satoh, H.; Aoki, M.; Takeda, M.; Hiromoto, N.; Inokawa, H. Fabrication and analytical modeling of integrated heater and thermistor for antenna-coupled bolometers. *Sens. Actuators A Phys.* **2015**, *222*, 160–166. [[CrossRef](#)]
48. Liu, W.; Asheghi, M. Thermal conduction in ultrathin pure and doped single-crystal silicon layers at high temperatures. *J. Appl. Phys.* **2005**, *98*, 123523. [[CrossRef](#)]
49. van Herwaarden, S. Physical principles of thermal sensors. *Sens. Mater.* **1996**, *8*, 373–387.
50. National Astronomical Observatory of Japan (Ed.) *Chronological Scientific Tables*; Maruzen: Tokyo, Japan, 2015.
51. Tiwari, A.; Satoh, H.; Aoki, M.; Takeda, M.; Hiromoto, N.; Inokawa, H. Analysis of Microbolometer Characteristics for Antenna-Coupled THz Detectors. *Asian, J. Chem.* **2013**, *25*, S358–S360.
52. Kraus, J.D.; Marhefka, R.J. *Antennas for All Applications*, 3rd ed.; McGraw-Hill Series in Electrical Engineering; McGraw-Hill: New York, NY, USA, 2002; Chapter 2; p. 35.
53. Harris, F.J. On the use of windows for harmonic analysis with the discrete Fourier transform. *Proc. IEEE* **1978**, *66*, 51–83. [[CrossRef](#)]

54. Pan, S.; Luo, Y.; Shalmany, S.H.; Makinwa, K.A.A. A Resistor-Based Temperature Sensor With a $0.13 \text{ pJ}\cdot\text{K}^2$ Resolution FoM. *IEEE J. Solid-State Circuits* **2018**, *53*, 164–173. [[CrossRef](#)]
55. Boukai, A.I.; Bunimovich, Y.; Kheli, J.T.; Yu, J.K.; Goddard, W.A.; Heath, J.R. Silicon nanowires as efficient thermoelectric materials. *Nature* **2008**, *451*, 168–171. [[CrossRef](#)]



© 2020 by the authors. Licensee MDPI, Basel, Switzerland. This article is an open access article distributed under the terms and conditions of the Creative Commons Attribution (CC BY) license (<http://creativecommons.org/licenses/by/4.0/>).